

Structural transformation of Sb-based high-speed phase-change material

Toshiyuki Matsunaga,^{a*} Rie Kojima,^b Noboru Yamada,^c Yoshiki Kubota^d and Kouichi Kifune^e

^aDevice Solutions Center, R&D Division, Panasonic Corporation, 3-1-1 Yagumo-Nakamachi, Moriguchi, Osaka 570-8501, Japan, ^bAVC Networks Company, Panasonic Corporation, 1-15 Matsuo-cho, Kadoma, Osaka 571-8504, Japan, ^cDepartment of Materials Science & Engineering, Kyoto University, Yoshidahonmachi, Sakyo-ku, Kyoto 606-8501, Japan, ^dGraduate School of Science, Osaka Prefecture University, 1-1 Gakuen-cho, Sakai, Osaka 599-8531, Japan, and ^eFaculty of Liberal Arts and Sciences, Osaka Prefecture University, 1-1 Gakuen-cho, Sakai, Osaka 599-8531, Japan

Correspondence e-mail:
matsunaga.toshiyuki@jp.panasonic.com

The crystal structure of a phase-change recording material (the compound $\text{Ag}_{3.4}\text{In}_{3.7}\text{Sb}_{76.4}\text{Te}_{16.5}$) enclosed in a vacuum capillary tube was investigated at various temperatures in a heating process using a large Debye–Scherrer camera installed in BL02B2 at SPring-8. The amorphous phase of this material turns into a crystalline phase at around 416 K; this crystalline phase has an A7-type structure with atoms of Ag, In, Sb or Te randomly occupying the 6c site in the space group. This structure was maintained up to around 545 K as a single phase, although thermal expansion of the crystal lattice was observed. However, above this temperature, phase separation into AgInTe_2 and Sb–Te transpired. The first fragment, AgInTe_2 , reliably maintained its crystal structure up to the melting temperature. On the other hand, the atomic configuration of the Sb–Te gradually varied with increasing temperature. This gradual structural transformation can be described as a continuous growth of the modulation period γ .

Received 28 March 2012

Accepted 20 September 2012

B-IncStrDB Reference:

6732EXfQbW

1. Introduction

Phase change recording is now extensively used for high-density non-volatile memories (Wuttig & Yamada, 2007). Since the 1970s, various materials have been proposed for this purpose, and today we have obtained two superior materials: GeTe– Sb_2Te_3 (GST) (Yamada *et al.*, 1991) and Sb–Te-based alloys such as $\text{Ag}_{3.4}\text{In}_{3.7}\text{Sb}_{76.4}\text{Te}_{16.5}$ (AIST or silver indium antimony tellurium; Iwasaki *et al.*, 1992); these materials are now practically used as the memory layers in phase-change optical disk media, as well as in the memory cells of solid-state electrical memories. Recording can be achieved using laser irradiation or ohmic heating to cause reversible phase changes between the amorphous and crystalline phases. We analyzed the crystal structure of AIST about 10 years ago (Matsunaga *et al.*, 2001), revealing that AIST has an A7-type structure, the same as that of pure Sb, in which four elements randomly occupy the 6c site in the space group. It has been presumed that this simple and spatially isotropic *p*–*p* connected six-coordination structure enables instantaneous transformation from the amorphous phase to the crystalline phase by minimal atomic rearrangement (Matsunaga *et al.*, 2006; Matsunaga, Yamada *et al.*, 2011). Our analysis also revealed that this A7-type quaternary crystal held its rhombohedral structure, showing a continuous atomic shift along the axis from $z = 0.233$ to $1/4$, when the temperature was raised close to the melting point. We examined the crystal structures of Sb–Te binary compounds, which are the mother alloys of the AIST materials, as well as those of Bi–Te compounds. These compounds are known, in thermal equilibrium, to have a series of commensurately or incommensurately modulated long-period layer structures, depending on their binary

compositions, between Sb and Sb_2Te_3 or between Bi and Bi_2Te_3 . Our present investigation of an as-deposited $\text{Ag}_{3.4}\text{In}_{3.7}\text{Sb}_{76.4}\text{Te}_{16.5}$ amorphous film in a sealed quartz tube revealed that when the temperature was raised, this quaternary alloy maintained an A7-type structure, hardly showing any atomic shift. However, decomposition into two phases, AgInTe_2 and Sb–Te, occurred at around 545 K. After this decomposition, the atomic configuration of the Sb–Te fragment with the A7-type disordered structure gradually moved into an ordered arrangement to finally obtain a stable homologous structure ruled by its composition. This can be considered as follows: the dopants, Ag and In, played roles in simplifying the structure of the quaternary alloy. However, once these dopants were lost, the structural feature of the Sb–Te binary compound revealed itself.

2. Experimental

A thin film of $\text{Ag}_{3.4}\text{In}_{3.7}\text{Sb}_{76.4}\text{Te}_{16.5}$ with a thickness of approximately 300 nm was formed by sputtering on a glass disk 120 mm in diameter. The film was scraped off with a spatula to create a powder, which was then packed into a quartz capillary tube with an internal diameter of 0.3 mm. To prevent it from reacting with components of air, we sealed the opening of the capillary tube using an oxyacetylene flame. The

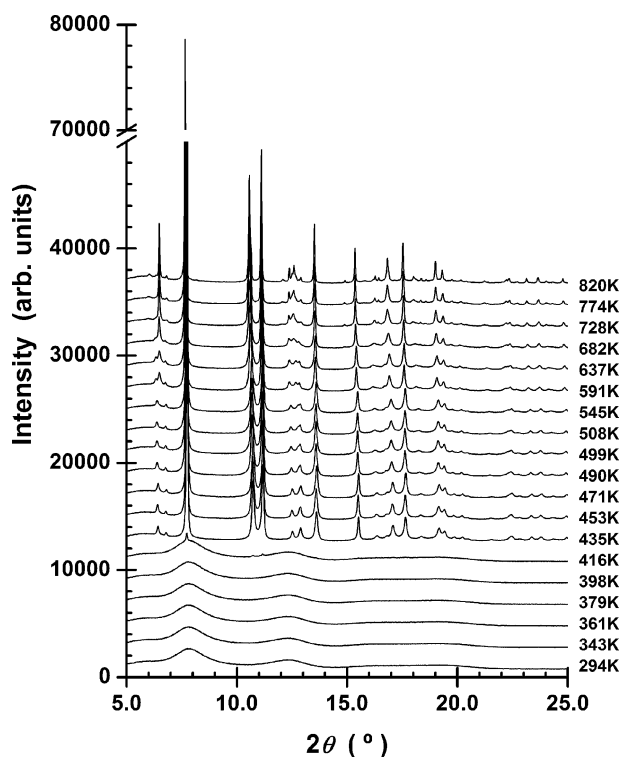


Figure 1 Temperature dependence of X-ray powder diffraction profiles for sputtered $\text{Ag}_{3.4}\text{In}_{3.7}\text{Sb}_{76.4}\text{Te}_{16.5}$ amorphous film in the heating process. The amorphous halo patterns are observed at low temperatures from 295 to 416 K. However, at around 416 K the Bragg peaks of the A7-type structure appear in the halo pattern. As the temperature is raised further, the A7-type single phase separates into two phases, AgInTe_2 and an Sb–Te binary compound, at around 545 K. At 2θ angles lower than 5° , Bragg peaks were hardly observed at any measurement temperatures.

Table 1

Final structural parameters for $\text{Ag}_{3.4}\text{In}_{3.7}\text{Sb}_{76.4}\text{Te}_{16.5}$ at 545 K refined by Rietveld analysis.

The standard deviations are shown in parentheses. The diffraction data used for the analysis: $5.50 \leq 2\theta \leq 31.50^\circ$. (a) Conventional three-dimensional Rietveld analysis results. The space group $R\bar{3}m$ was applied. (b) Results of a four-dimensional superspace analysis refined as a commensurately modulated structure, using the ‘commensurate case’ in the refinement program *JANA*; the modulation period γ was maintained at $3/2$ during the refinements (the analysis assuming an incommensurate case also concluded that this crystal has a commensurate structure with $\gamma = 3/2$). The superspace group was assumed to be $R\bar{3}m(00\gamma)00$ (de Wolff, 1974; de Wolff *et al.*, 1981). B_i^j represents the positional modulation amplitude. The determined z -slope (the form factor of the sawtooth function) value corresponds to $z = 0.2359$ in the three-dimensional description; this z value shows good agreement with $z = 0.2365$, which was derived from the three-dimensional analysis. U^{ij} represent the atomic displacement parameters. It was assumed that the four atoms randomly occupy the atomic sites in both analyses.

(a) $R_p = 0.0215$, $R_{wp} = 0.0313$, $RF_{obs} = 0.0157$, $RF_{wobs} = 0.0238$, $a = 4.3037$ (5) and $c = 11.290$ (1) Å. M : $\text{Ag}_{0.034}\text{In}_{0.037}\text{Sb}_{0.764}\text{Te}_{0.165}$.

Atom	Site	g	x	y	z	U^{11} (Å ²)	U^{33} (Å ²)
M	6c	1.0	0	0	0.2365 (1)	0.0235 (5)	0.042 (2)

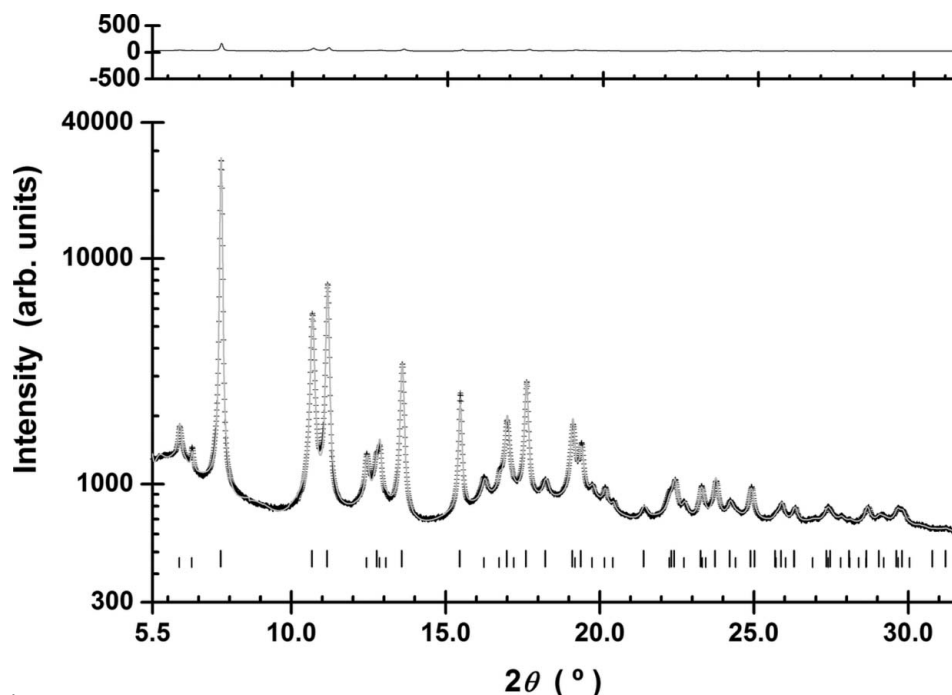
(b) Commensurate case ($t_0 = \frac{1}{4}, \frac{3}{4}$).

R factors of profile and all reflections		
	R_p	0.0202
	R_{wp}	0.0292
	RF_{obs}	0.0133
	RF_{wobs}	0.0198
R factors of main and satellite reflections		
Main	RF_{obs}	0.0111
	RF_{wobs}	0.0141
R factors of satellites		
First-order	RF_{obs}	0.0184
	RF_{wobs}	0.0273

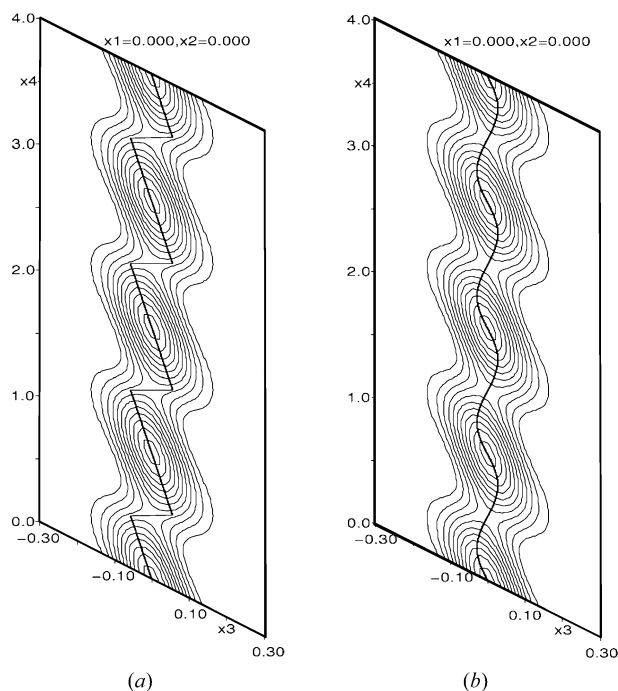
$\gamma = 3/2$; $a = 4.3037$ (5), $c = 5.6452$ (6) Å

Atom	g	x	y	z	z -slope	U^{11} (Å ²)	U^{33} (Å ²)
M	1.0	0	0	0	−0.0563 (8)	0.0229 (5)	0.043 (1)

diffraction experiments were carried out using the large-diameter Debye–Scherrer camera with an imaging plate on the BL02B2 beamline at the Japan Synchrotron Radiation Research Institute (Nishibori *et al.*, 2001). The energy of the incident beam was approximately 29.4 keV. An imaging plate with a pixel area of $100 \mu\text{m}^2$ was used as the detector; this pixel area corresponded to an angular resolution of 0.02° (287 mm camera diameter). However, for more precise structure analyses, intensity data in increments of 0.01° were obtained by reading the imaging plate for a pixel area of $50 \mu\text{m}^2$. Experiments at low and high temperatures were carried out while blowing nitrogen gas onto the capillary tube at the specified temperatures. The crystal structures were examined and refined using the Rietveld method (Rietveld, 1969); the programs *JANA2000* (Petříček & Dušek, 2000) and *JANA2006* (Petříček *et al.*, 2006) were used for this purpose. The energy of the synchrotron radiation was confirmed by recording the diffraction intensity of CeO_2 ($a = 5.4111$ Å) powder as a reference specimen at room temperature under


Figure 2

Observed (+) and calculated (gray line) X-ray diffraction profiles for $\text{Ag}_{3.4}\text{In}_{3.7}\text{Sb}_{76.4}\text{Te}_{16.5}$ (crystallized into an A7-type single structure) at 545 K by four-dimensional Rietveld analysis in the commensurate case. A difference curve (observed – calculated) appears at the top of the figure; reflection markers are indicated by vertical spikes below the diffraction patterns: the longer ones are for the peaks of the main reflections and the shorter ones for the satellites.


Figure 3

Electron-density maps for $\text{Ag}_{3.4}\text{In}_{3.7}\text{Sb}_{76.4}\text{Te}_{16.5}$ at 545 K depicted with F_o ; only positive contours are drawn at intervals of $200 \text{ e} \text{ \AA}^{-3}$. (a) The sawtooth-type modulation function used to describe the displacement of the atom in an asymmetric unit of this three-dimensional crystal is indicated by a solid line. As seen by comparison with map (b) obtained from the Rietveld analysis with a harmonic function, analysis with the sawtooth function provided better results.

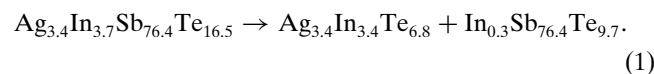
the same conditions, which showed that the wavelength used for the structural analyses was $0.4187(3) \text{ \AA}$. Neutral atomic scattering factors were employed for them.

3. Results and discussion

3.1. Crystals observed in this experiment

The diffraction patterns obtained for the sputtered $\text{Ag}_{3.4}\text{In}_{3.7}\text{Sb}_{76.4}\text{Te}_{16.5}$ amorphous film are shown in Fig. 1. The amorphous phase transformed into an A7-type crystalline single phase, as seen in this graph, at around 416 K. The results of a search match and Rietveld analyses revealed the diffraction patterns taken from 435 to 545 K to be almost identical to that of an As, Sb or Bi crystal with an A7-type structure (Clark, 1955), as has been previously elucidated (Matsunaga *et al.*, 2001). The (conventional three-dimensional)

Rietveld analysis results at 545 K are shown in Table 1(a). This crystal belongs to the space group $R\bar{3}m$; the four constituent elements, Ag, In, Sb and Te, randomly occupy the 6c site (Matsunaga, Akola *et al.*, 2011). The changes in the diffraction lines with increasing temperature show that the single-phase A7-type structure is maintained up to around 545 K. However, the peaks for CuFeS₂-type AgInTe_2 (Wyckoff, 1986) appear at around 590 K, along with those of the A7-type structure. This decomposition can be written as



These two phases formed by heating coexisted up to the high temperatures at which their Bragg peaks almost disappeared as a result of dissolving. As seen in this equation, the second decomposition product can virtually be regarded as an Sb–Te binary compound. Even at high temperatures close to the melting temperature, AgInTe_2 tightly held the CuFeS₂-type structure irrespective of temperature. However, our present analysis revealed that the structure of the second fragment, the Sb–Te compound, gradually changed with increasing temperature until obtaining its final stable atomic configuration. These structures can be closely approximated by the A7-type structure but are not real A7-type ones.

3.2. Homologous structures

We examined many types of chalcogenide materials to clarify the high-speed phase-change mechanism and develop

Table 2

Space groups for $(\text{GeTe})_n(\text{Sb}_2\text{Te}_3)_m$ pseudobinary compounds.

N shows the number of atomic layers in the unit cell.

Compound	n	m	N	Space group
$\text{Ge}_3\text{Sb}_2\text{Te}_6$	3	1	33	$R\bar{3}m$
$\text{Ge}_2\text{Sb}_2\text{Te}_5$	2	1	9	$P\bar{3}m1$
$\text{Ge}_1\text{Sb}_2\text{Te}_4$	1	1	21	$R\bar{3}m$
$\text{Ge}_1\text{Sb}_4\text{Te}_7$	1	2	12	$P\bar{3}m1$
$\text{Ge}_1\text{Sb}_6\text{Te}_{10}$	1	3	51	$R\bar{3}m$

new materials for future ultra-high-density phase-change recording devices. This revealed that, after sufficient heat treatments, almost all these materials finally fell into their stable crystals with so-called homologous structures. It has been found that in thermal equilibrium, the typical phase-change materials, the GeTe– Sb_2Te_3 pseudobinary system, the Sb–Te or Bi–Te binary system, form various intermetallic compounds represented by the chemical formulae $(\text{GeTe})_n(\text{Sb}_2\text{Te}_3)_m$, $(\text{Sb}_2)_n(\text{Sb}_2\text{Te}_3)_m$ or $(\text{Bi}_2)_n(\text{Bi}_2\text{Te}_3)_m$ (n, m : integer). All these compounds have trigonal structures with $2n + 5m$ cubic close-packed periodicity (almost) without exception. [More specifically, the residual of $(2n + 5m)/3 = 0$ and $\neq 0$ leads to the formation of crystals having structures with primitive (P) and rhombohedral (R) unit cells; they form structures with $N = (2n + 5m)$ and $N = 3 \cdot (2n + 5m)$ layers, respectively.] Table 2 shows the case of the GeTe– Sb_2Te_3 compounds; all of the existing intermetallic compounds in these systems follow this rule (Matsunaga & Yamada, 2004a; Matsunaga, Yamada & Kubota, 2004; Matsunaga *et al.*, 2007a,b, 2010; Matsunaga, Kojima *et al.*, 2008). This could also be confirmed from the relevant tables in other papers (Karpinsky *et al.*, 1998; Kuznetsova *et al.*, 2000; Shelimova *et al.*, 2000, 2004; Shelimova, Karpinskii *et al.*, 2001; Shelimova, Konstantinov *et al.*, 2001; Poudeu & Kanatzidis, 2005). These structures are similar to each other and systematically characterized by the stacking of the $(\text{GeTe})_n$ and $(\text{Sb}_2\text{Te}_3)_m$, $(\text{Sb}_2)_n$ and $(\text{Sb}_2\text{Te}_3)_m$, or $(\text{Bi}_2)_n$ and $(\text{Bi}_2\text{Te}_3)_m$ blocks along the c_H axes, with very long cell dimensions in the conventional three-dimensional structure description (Karpinsky *et al.*, 1998; Shelimova *et al.*, 2000; Shelimova, Karpinskii *et al.*, 2001; Poudeu & Kanatzidis, 2005; Matsunaga & Yamada, 2004a, Matsunaga, Yamada & Kubota, 2004; Matsunaga *et al.*, 2007a,b, 2010; Matsunaga, Kojima *et al.*, 2008; Matsunaga, Morita *et al.*, 2008). More generally and more precisely it has been assumed that these structures should be described as commensurately or incommensurately modulated four-dimensional structures characterized by modulation vectors $\mathbf{q} = \gamma \cdot \mathbf{c}^*$ (Lind & Lidin, 2003), where γ values are real numbers equal to or around $3(n + 3m)/(2n + 5m)$ [see equation (3)]; \mathbf{c}^* is the fundamental reciprocal vector formed by three-layer cubic stacking]. For instance, it has been clarified that, in the thermal equilibrium, Sb_8Te_3 ($n = 3$ and $m = 1$) has a homologous structure characterized by a modulation vector $\mathbf{q} = 18/11 \cdot \mathbf{c}^*$ (Kifune *et al.*, 2005, 2011). Thus, we applied this more universal four-dimensional superspace method for

Table 3

Final structural parameters.

(a) Final structural parameters determined by four-dimensional superspace refinements of $\text{Sb}_{89}\text{Te}_{11}$ and conventional three-dimensional refinements of AgInTe_2 at room temperature. The R factors for the entire pattern ($\text{Sb}_{89}\text{Te}_{11} + \text{AgInTe}_2$) are $R_p = 0.0205$ and $R_{wp} = 0.0297$. The superspace group for $\text{Sb}_{89}\text{Te}_{11}$ was assumed to be $R\bar{3}m(00\gamma)00$; on the other hand, $I42d$ was applied for AgInTe_2 . Both structures were refined simultaneously using a multiphase refinement. Diffraction data used for the analysis: $5.50 \leq 2\theta \leq 42.10^\circ$. The standard deviations are shown in parentheses. B_n^i represents the positional modulation amplitude, whereas U_s represent the atomic displacement parameters. (b) and (c) Final structural parameters obtained by four-dimensional superspace refinements of $\text{Sb}_{89}\text{Te}_{11}$ performed by applying sawtooth functions (Dušek *et al.*, 2010) or harmonic functions orthogonalized to the crenel interval (Lind & Lidin, 2003) instead of conventional harmonic functions. The R factors for the entire pattern ($\text{Sb}_{89}\text{Te}_{11} + \text{AgInTe}_2$) are $R_p = 0.0205$ and $R_{wp} = 0.0297$, and $R_p = 0.0204$ and $R_{wp} = 0.0298$. (d) The results obtained by the four-dimensional Rietveld analyses performed assuming that $\text{Sb}_{89}\text{Te}_{11}$ has a commensurately modulated structure; the modulation period γ was maintained at $45/29$ during the refinements. The R factors for the entire pattern are $R_p = 0.0202$ and $R_{wp} = 0.0295$. The superspace group was assumed to be the same as in the above incommensurate case. The electron density map and atomic positions obtained from this analysis in the commensurate case are not shown in this paper, but were almost identical to those seen in Fig. 6. Only the first- and second-order satellites were considered for these four-dimensional analyses ($f = 0, 1$ and 2 were used for the analyses). This assumption gave sufficiently low R values.

(a) $\text{Sb}_{89}\text{Te}_{11}$:

R factors of profile and all reflections			
	RF_{obs}		0.0162
	RF_{wobs}		0.0159
R factors of main and satellite reflections			
Main	RF_{obs}		0.0144
	RF_{wobs}		0.0158
R factors of satellites			
First order	RF_{obs}		0.0186
	RF_{wobs}		0.0196
Second order	RF_{obs}		0.0138
	RF_{wobs}		0.0132

$\gamma = 1.5516$ (4); $a = 4.2969$ (1), $c = 5.6759$ (2) Å.

Atom	g	x	y	z	B_1^i	B_2^i	U^{11} (Å ²)	U^{33} (Å ²)
Sb	1.0	0	0	0	−0.0394 (4)	0.003 (1)	0.0123 (2)	0.0101 (7)
Te	1.0	0	0	0	−0.27 (1)	–	0.0123	0.0101

AgInTe_2 : $RF_{\text{obs}} = 0.0253$, $RF_{\text{wobs}} = 0.0281$, $a = 6.4275$ (3) and $c = 12.6089$ (9) Å.

Atom	Site	g	x	y	z	U_{iso} (Å ²)
Ag	4b	1/4	0	0	1/2	0.029
In	4a	1/4	0	0	0	0.029
Te	8d	1/2	0.252 (11)	1/4	1/8	0.029 (1)

(b) $\text{Sb}_{89}\text{Te}_{11}$:

R factors of profile and all reflections			
	RF_{obs}		0.0168
	RF_{wobs}		0.0176
R factors of main and satellite reflections			
Main	RF_{obs}		0.0123
	RF_{wobs}		0.0136
R factors of satellites			
First order	RF_{obs}		0.0221
	RF_{wobs}		0.0238

Table 3 (continued)

Second order	RF_{obs}		0.0141					
	RF_{wobs}		0.0152					
$\gamma = 1.5511$ (4); $a = 4.2968$ (1), $c = 5.6758$ (2) Å.								
Atom	<i>g</i>	<i>x</i>	<i>y</i>	<i>z</i>	B_1^i	z-slope	U^{11} (Å ²)	U^{33} (Å ²)
Sb	1.0	0	0	0	−0.0345 (3)	−0.009 (4)	0.0122 (2)	0.0102 (9)
Te	1.0	0	0	0	—	0.095 (5)	0.0122	0.0102
AgInTe ₂ : $RF_{\text{obs}} = 0.0227$, $RF_{\text{wobs}} = 0.0266$, $a = 6.4275$ (3) and $c = 12.6079$ (9) Å.								
Atom	Site	<i>g</i>	<i>x</i>	<i>y</i>	<i>z</i>	U_{iso} (Å ²)		
Ag	4 <i>b</i>	1/4	0	0	1/2	0.029		
In	4 <i>a</i>	1/4	0	0	0	0.029		
Te	8 <i>d</i>	1/2	0.26 (5)	1/4	1/8	0.029 (1)		

(c) Sb₈₉Te₁₁:

R factors of profile and all reflections		RF_{obs}	0.0156
		RF_{wobs}	0.0164
R factors of main and satellite reflections			
Main	RF_{obs}	0.0115	
	RF_{wobs}	0.0128	
R factors of satellites			
First order	RF_{obs}	0.0202	
	RF_{wobs}	0.0218	
Second order	RF_{obs}	0.0141	
	RF_{wobs}	0.0142	

$\gamma = 1.5511$ (4); $a = 4.2968$ (1), $c = 5.6759$ (2) Å.

Atom	<i>g</i>	<i>x</i>	<i>y</i>	<i>z</i>	Zort1	Zort3	U^{11} (Å ²)	U^{33} (Å ²)
Sb	1.0	0	0	0	−0.0314 (3)	−0.001 (1)	0.0122 (2)	0.0102 (8)
Te	1.0	0	0	0	−0.049 (3)	—	0.0122	0.0102
AgInTe ₂ : $RF_{\text{obs}} = 0.0227$, $RF_{\text{wobs}} = 0.0257$, $a = 6.4274$ (3) and $c = 12.6084$ (9) Å.								
Atom	Site	<i>g</i>	<i>x</i>	<i>y</i>	<i>z</i>	U_{iso} (Å ²)		
Ag	4 <i>b</i>	1/4	0	0	1/2	0.028		
In	4 <i>a</i>	1/4	0	0	0	0.028		
Te	8 <i>d</i>	1/2	0.255 (6)	1/4	1/8	0.028 (1)		

(d) Commensurate case ($t_0 = \frac{1}{50} + \frac{n}{25}$; $n = 0, 1, 2, \dots$). Sb₈₈Te₁₁:

R factors of profile and all reflections		RF_{obs}	0.0158
		RF_{wobs}	0.0159
R factors of main and satellite reflections			
Main	RF_{obs}	0.0135	
	RF_{wobs}	0.0150	
R factors of satellites			
First order	RF_{obs}	0.0182	
	RF_{wobs}	0.0197	
Second order	RF_{obs}	0.0160	
	RF_{wobs}	0.0137	

$\gamma = 45/29$; $a = 4.2968$ (1), $c = 5.6758$ (2) Å.

Table 3 (continued)

Atom	<i>g</i>	<i>x</i>	<i>y</i>	<i>z</i>	B_1^i	B_2^i	U^{11} (Å ²)	U^{33} (Å ²)
Sb	1	0	0	0	−0.0401 (4)	0.001 (1)	0.0119 (2)	0.0107 (9)
Te	1	0	0	0	−0.31 (2)	—	0.0119	0.0107
AgInTe ₂ : $RF_{\text{obs}} = 0.0241$, $RF_{\text{wobs}} = 0.0273$, $a = 6.4276$ (3) and $c = 12.6082$ (9) Å.								
Atom	Site	<i>g</i>	<i>x</i>	<i>y</i>	<i>z</i>	U_{iso} (Å ²)		
Ag	4 <i>b</i>	1.0	0	0	1/2	0.028		
In	4 <i>a</i>	1.0	0	0	0	0.028		
Te	8 <i>d</i>	1.0	0.254 (7)	1/4	1/8	0.028 (1)		

analysis of the Sb–Te compound formed by thermal decomposition [see equation (1)].

3.3. Structures of Ag_{3.4}In_{3.7}Sb_{76.4}Te_{16.5} and Sb₈₉Te₁₁ compounds

As the initial structure models for the four-dimensional Rietveld refinements we adopted the layer stacking structures defined by the respective γ values. In other words, in the Sb–Te compounds examined in this study, the modulation functions for Sb and Te atoms were respectively distributed around $t = 0$ and $t = 1/2$ (t : internal parameter along the x_4 axis, the fourth crystal axis in four-dimensional space; Lind & Lidin, 2003). This corresponds to a structure in which Sb and Te are placed at 0, 0, 0 and their atomic species are distinguished using crenel functions (for Sb₈₉Te₁₁, width: 0.89 + center: 0 for Sb and width: 0.11 + center: 0.5 for Te). As there is a difference of only one between the atomic numbers of Sb⁵¹ and Te⁵², it is very difficult for us to distinguish the kinds of atoms in their unit cells. We use the assumption that all of the Sb–Te crystals examined in this study have perfectly ordered atomic arrangements like those of other (binary) systems. The intensities of the satellites for Sb–Te compounds are rather weak in general. Those of Sb₈₉Te₁₁ are no exception; almost all of the satellites observed were reproduced by adopting the maximum satellite index of 2 for the Rietveld analyses. The atomic displacements were represented using harmonic functions.

The four-dimensional Rietveld analyses performed with the diffraction patterns in Fig. 1, as mentioned above, provided the structural dependence on the temperature for Ag_{3.4}In_{3.7}Sb_{76.4}Te_{16.5} (at low temperatures) and its thermally decomposed materials (at high temperatures). The results of the Rietveld analyses at 545 K for Ag_{3.4}In_{3.7}Sb_{76.4}Te_{16.5}, whose crystal still maintains an A7-type structure, are shown in Table 1(b) and Fig. 2 (*cf.* Table 1a, from the three-dimensional Rietveld analysis). In the four-dimensional analysis for this crystal, displacement for only a single atom in a three-dimensional asymmetric unit has to be described by selecting the appropriate one from among several kinds of modulation functions; in this case, the use of a sawtooth function (Dušek *et al.*, 2010) was revealed to give better results than a harmonic function, as seen in Fourier maps based on F_o (Fig. 3). We can see from Fig. 4, γ maintained a constant value of 1.5 up to a

temperature of around 590 K, at which AgInTe₂ came out. However, above this temperature, γ grew larger with increasing temperature and reached a value of around 1.55 at high temperatures near the melting point of Sb_{76.4}Te_{9.7} (= Sb_{88.7}Te_{11.3} when expressed as a percentage), which was found at around 870 K according to our present high-temperature measurement. The γ value was maintained at around 1.55 even when the powder specimen was cooled back to room temperature. The results of the Rietveld analysis at room temperature are shown in Table 3(a) and Fig. 5. The refined modulation functions of Sb and Te and the corresponding de Wolff section of the observed Fourier map are shown in Fig. 6(a), together with a Fourier map based on F_0 . The difference Fourier maps obtained from the determined structure models exhibited few significant residual peaks, which showed the need for further structural modification or improvement. This was similar to those obtained at the high temperatures of 774 and 820 K. The γ values of around 1.55 found in these stagnated structures correspond well with the value of 1.5565 expected from the composition of Sb_{88.7}Te_{11.3}. Here we can simply derive γ in terms of x as

$$\gamma = 2 - x/2, \quad (2)$$

when the chemical formula for the binary system is written as Sb _{x} Te_{1- x} or Bi _{x} Te_{1- x} (Lind & Lidin, 2003). It can be considered that after Sb_{76.4}Te_{9.7} was segregated from AgInTe₂, it revealed its original crystalline nature to change the layer period (γ) from 1.5 ($n = 1, m = 0$; A7-type six-layer structure) to 1.55 (another long-period layer structure), and it also clarified that, surprisingly enough, even an Sb–Te compound with as much as 89% Sb can exist as a single homologous structure in its binary system. We can obtain

$$\gamma = 3(n + 3m)/(2n + 5m) \text{ and } x = 2(n + m)/(2n + 5m), \quad (3)$$

by comparing Sb _{x} Te_{1- x} with (Sb₂) _{n} (Sb₂Te₃) _{m} . The crystal structure ($\gamma \simeq 1.55$) at high temperatures at which the γ growth became stagnant can be approximated reasonably well by a commensurately modulated 29-layer structure with $n = 12$ and $m = 1$ ($\gamma = 45/29$; this three-dimensional structure model is shown in Fig. 7a). We also carried out a Rietveld analysis assuming that this Sb–Te crystal had a commensurately modulated structure with this rational number of γ . As shown in Table 3(d), this analysis gave almost the same good results as in the incommensurate case (however, for this material it could not be concluded that it had transformed to a commensurate three-dimensional structure, in contrast to Sb₈₇Te₁₃, which will be discussed later). The Fourier map obtained from this four-dimensional analysis performed in the commensurate case is almost identical with all those in Fig. 6, as expected. In addition to the γ dependence on temperature of this Sb–Te material, the Sb₈Te₃ sputtered amorphous film showed a small γ value just after the transformation to the crystalline phase. However, γ became larger with increasing temperature to finally obtain its original long-period layer structure. We found that, in addition to the Sb₈Te₃ film, some other Sb–Te films at various compositions show very similar

behavior (we will show the results for these materials elsewhere in the near future). These results strongly suggest that not a few (at least) Sb–Te compounds, just after their crystal formations, transiently assume small γ values (it is highly probable that these γ values all start at 3/2), and when adequately treated with heat, they become larger to attain their respective, intrinsic homologous structures, depending on their binary compositions.

The atomic displacements (modulation functions) have already been shown in a stagnant structure of Sb₈₉Te₁₁ (see Fig. 6). However, just after the phase decomposition, the atomic displacements varied appreciably, as seen in Fig. 8. This figure shows, however, that such a varied atomic arrangement becomes more moderate with increasing temperature, and comes closer to those observed in the stagnated structures. In response to this structural change, although the interatomic distances in Sb₈₉Te₁₁ just after the phase decomposition are rather dispersed, especially for Te–Sb pairs, they converge with the structural inactivation, as seen in Fig. 9. As mentioned above, before the phase decomposition, Sb and Te atoms (and the dopants) were randomly distributed in the A7-type structure. Therefore, it is expected that just after the decomposition, the crystal still has a strongly disordered atomic arrangement. However, during the structural change with increasing temperature, it gradually attains the perfectly ordered structure shown above (Kifune *et al.*, 2011).

As mentioned above, we used harmonic functions to describe the atomic displacements. However, to examine them more precisely, the JANA2006 program provides several other functions in addition to the harmonic one. We performed further analyses by using some of these functions. However, these analyses gave us almost the same results as shown in Fig. 6 and Tables 3(b) and (c).

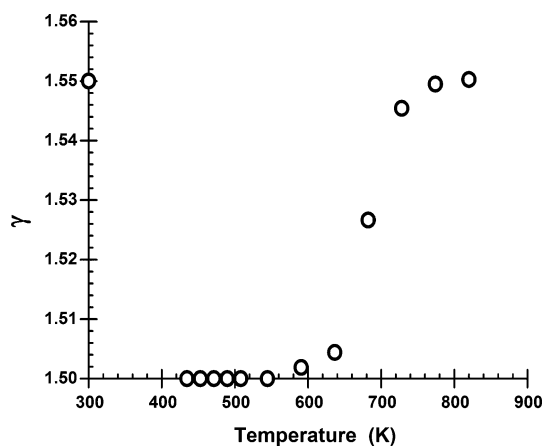


Figure 4 Temperature dependences of modulation period γ obtained from four-dimensional structural analyses. The diffraction measurements were first made in the heating process up to 820 K; then the powder specimen was cooled down for a room-temperature measurement. Error bars were omitted because they were smaller than the symbols shown.

3.4. Suitability of Sb–Te-based compounds for high-speed phase-change recording devices

As has so far been shown, an Sb–Te compound containing Ag and In maintains a six-layer structure ($\gamma = 3/2$) up to a high temperature, at which phase separation occurs. On the other

hand, Sb–Te films without such dopants show γ values larger than

$3/2$ immediately after the crystallization. This strongly suggests that the Ag and In dopants play roles in maintaining the simple structure of the Sb–Te matrix. It also inversely implies that every Sb–Te binary-compound film will experience a six-

layer structure in a very short time right after the crystal formation because six layers is the simplest and shortest layer structure out of all of the possible homologous structures from Sb ($\gamma = 3/2$) to Sb_2Te_3 ($\gamma = 9/5$). Many studies (for instance, Matsunaga, Akola *et al.*, 2011) have shown that phase-change chalcogenide amorphous materials have spatially isotropic atomic arrangements; it is highly likely that they crystallize once into simple and spatially isotropic structures, like a cubic crystal, because a six-layer (A7-type) structure can be well approximated by simple cubic lattices (Matsunaga & Yamada, 2004b).

The atomic configuration in the amorphous phase of this material, which has already been revealed (Matsunaga, Akola *et al.*, 2011), is highly disordered, similar to that of a liquid, and spatially has a completely isotropic symmetry. However, it has also been revealed that it has 3 + 3 coordination structures even in such a disordered atomic arrangement, as well as that of the crystalline phase: that is, both phases have very similar coordination structures, *i.e.* locally very similar atomic arrangements (it is well known that an A7-type crystal has a 3 + 3 coordination structure; Clark, 1955; Hoffmann, 1988). This is one of the major reasons that this material achieves a sufficiently high phase-change speed by locally minimal bond interchanges. As for the dopants, it has been presumed that either or both Ag and In atoms probably raise the crystallization temperature of the amorphous phase to obtain a sufficient endurance for long-term data preservation. In addition, as mentioned above, they make the atomic arrangement of the crystal simple and spatially isotropic, holding the

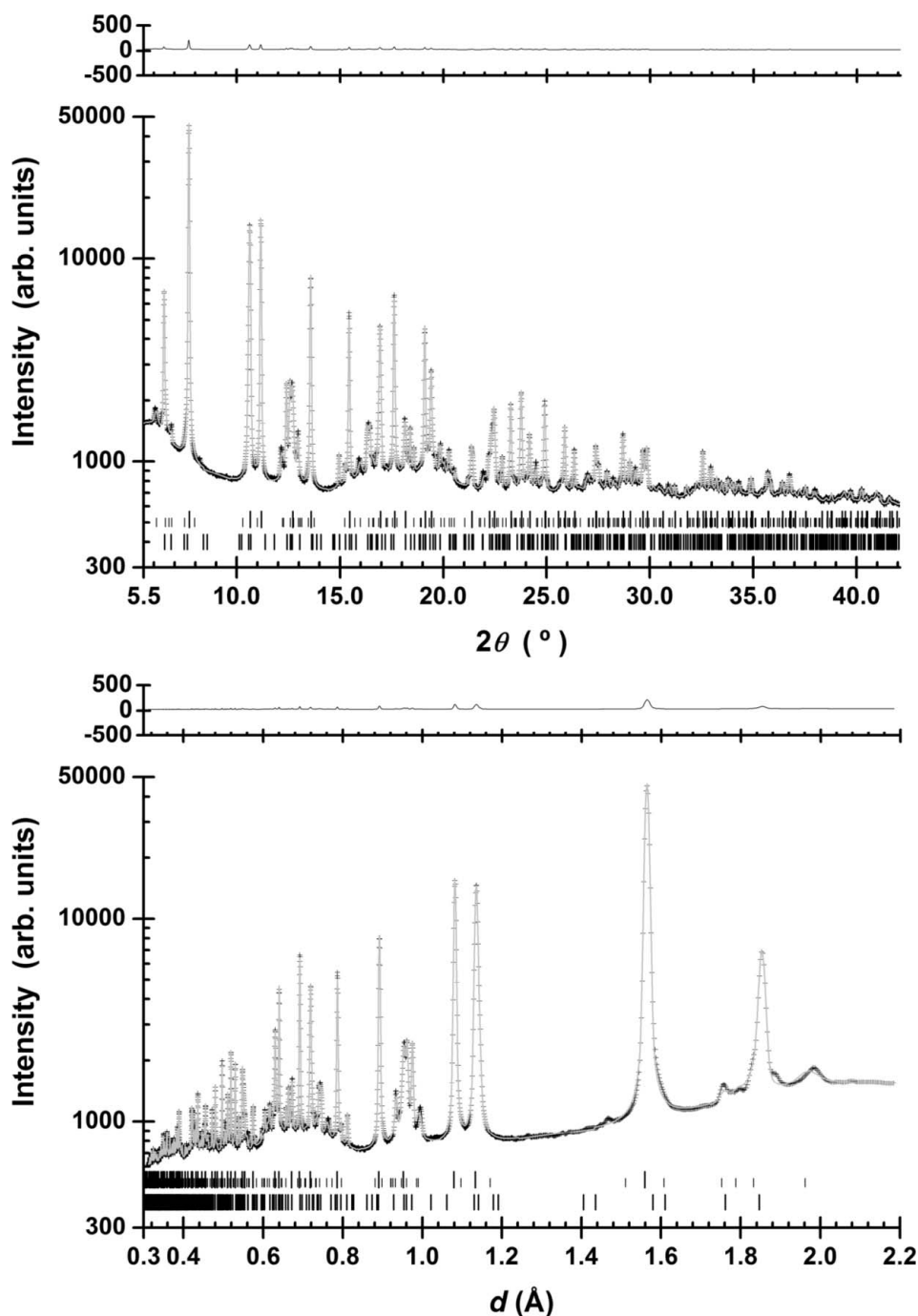


Figure 5

Observed (+) and calculated (gray line) X-ray diffraction profiles for $\text{AgInTe}_2 + \text{Sb}_{89}\text{Te}_{11}$ at room temperature by Rietveld analysis. A difference curve (observed–calculated) appears at the top of the figure; reflection markers are indicated by vertical spikes below the diffraction patterns. Of the first line of spikes, the longer ones are for the peaks of the main reflections of $\text{Sb}_{89}\text{Te}_{11}$, and the shorter ones are for the satellites. Those at the bottom show the peak positions for AgInTe_2 . As seen in the figure depicted in d spacing, a few unmatched weak peaks were observed, which were presumed to be from another contaminant phase.

Table 4

Final structural parameters and *R* factors.

(a) Final structural parameters for $\text{Ag}_{3.4}\text{In}_{3.7}\text{Sb}_{76.4}\text{Te}_{16.5}$ refined using conventional three-dimensional Rietveld analyses. In these analyses it was assumed that this material kept an unchanged A7-type structure while AgInTe_2 formed at around 590 K with increasing temperature. The space group $R\bar{3}m$ was applied to all structure models, despite the fact that for $z = 1/4$ $R\bar{3}m$ or $R32$ should be used instead (Matsunaga *et al.*, 2001). The standard deviations are shown in parentheses, and the reliability factors are indicated as percentages. (b) The *R*-factors (shown as percentages) obtained through the four-dimensional analyses (see Table 5a) are also tabulated for comparison.

(a)				(b)			
<i>T</i> (K)	<i>a</i> (Å)	<i>c</i> (Å)	<i>z</i>	<i>RF</i> _{obs}	<i>RF</i> _{wobs}	<i>RF</i> _{obs}	<i>RF</i> _{wobs}
435	4.3010 (6)	11.202 (2)	0.2356 (1)	1.37	1.83		
453	4.3013 (6)	11.212 (2)	0.2359 (1)	1.47	2.15		
471	4.3015 (6)	11.223 (2)	0.2360 (1)	1.90	2.15		
490	4.3019 (6)	11.242 (2)	0.2362 (1)	2.06	2.35		
508	4.3033 (6)	11.267 (2)	0.2364 (1)	1.73	2.33		
545	4.3037 (5)	11.290 (1)	0.2365 (1)	1.57	2.38		
591	4.3084 (1)	11.330 (1)	0.2365 (1)	1.80	2.36	1.71	1.82
637	4.3094 (3)	11.357 (1)	0.2373 (1)	1.84	2.02	1.49	1.71
682	4.3110 (4)	11.399 (1)	0.2400 (1)	2.37	2.79	1.23	1.29
728	4.3127 (3)	11.438 (1)	0.2460 (4)	2.65	3.60	1.43	1.45
774	4.3159 (3)	11.439 (1)	0.25	2.25	2.14	1.60	1.74
820	4.3202 (3)	11.429 (1)	0.25	1.94	1.81	1.75	1.78

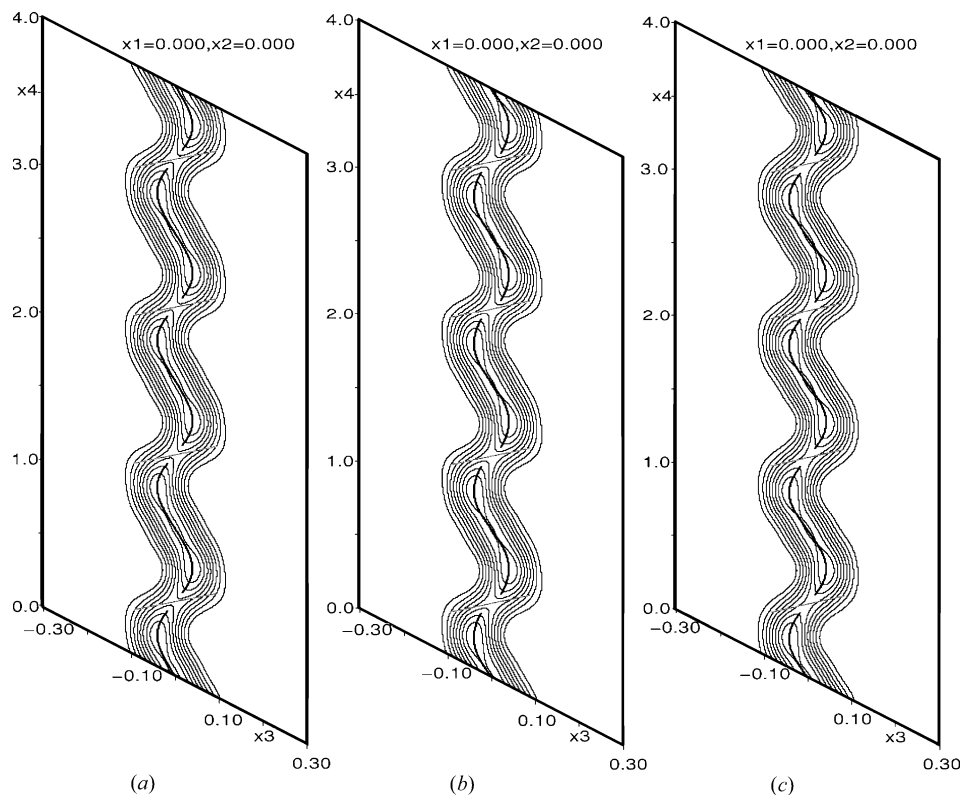


Figure 6

Electron-density maps for $\text{Sb}_{80}\text{Te}_{11}$ at room temperature based on F_o ; only positive contours are drawn at intervals of $500 \text{ e} \text{ \AA}^{-3}$. These maps, (a), (b) and (c), correspond to the results obtained from three kinds of the Rietveld analyses, (a), (b) and (c), shown in Table 3. The crystal obtained a stagnant atomic arrangement after high-temperature measurements. These maps are almost identical to Fourier maps based on F_c . The modulations in the displacement of the two atoms in this binary alloy are indicated by the crossing curves for Sb in black and for Te in gray. These were analyzed by using different functions to describe the atomic displacement; however, we can see that they are almost the same.

material in a single phase. It is expected that these are indispensable features for high-speed rewritable data storage media. In the near future, however, the individual roles played by Ag and In in the phase change of this material should be clarified.

3.5. Three- or six-layer structure approximation for Sb–Te compounds

In our previous work (Matsunaga *et al.*, 2001) Sb–Te compounds with small amounts of Ag or In were concluded to hold an A7-type structure up to the melting point. However, we must say that these compounds do not have an exact A7-type structure but a long-period modulated structure defined by the binary composition in thermal equilibrium. The A7-type (six-layer) structure is also one of the modulated structures (corresponding to the shortest period one). All the above-mentioned modulated structures can be approximated by a (cubic stacked) three-layer structure, which provides the fundamental lines in the diffraction patterns. If atoms at the 6c site are located at $z = 1/4$ in the A7-type structure, it corresponds to the three-layer structure. In the previous temperature measurement, one end of the capillary holding the

powder specimen was open to the air, which yielded not a little Sb oxide (Fig. 10). This oxide formed a line of unnecessary Bragg peaks, which hindered us from determining the (weak) satellite peaks identifying the layer period of the structure. Further, at that time, such modulated structures were not familiarly associated with the Sb–Te binary system. All these factors made it difficult for us to discern that these Sb–Te-based alloys can take modulated structures. Thus, in previous work the A7-type structure was exclusively applied in the structural analyses, irrespective of the measurement temperature, which provided apparently sufficient results. In addition, in this work the same structural analysis was carried out to confirm the reproducibility of the previous work; we analyzed the structures by applying this simple 6R structure to them. The results are shown in Table 4. As shown in this table, the *R* factors were sufficiently low and the positional parameter *z* gradually increased with temperature (which meant that the structure model for the Rietveld analysis gradually became

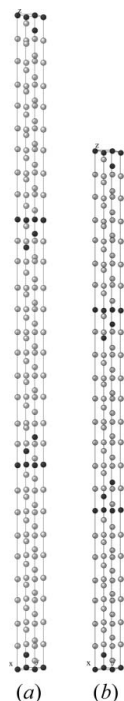


Figure 7
Structural models of (a) $\text{Sb}_{26}\text{Te}_3$ and (b) $\text{Sb}_{20}\text{Te}_3$. The atomic positions of Sb and Te are shown by gray and black, respectively.

closer to the three-layer structure), which accurately reproduced the previous results. However, the agreement between the profiles of the observed and calculated intensities became worse as the temperature rose, especially for the (weak)

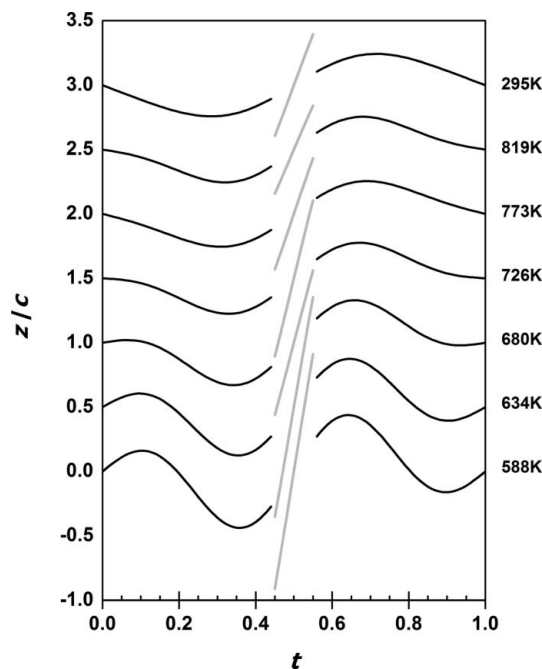


Figure 8
Displacements of z as a function of t . Each profile is shifted by $dz = 0.5$ with respect to the previous one (horizontal lines correspond to $dz = 0$ for each group of profiles). The centers of modulation functions of Sb and Te atoms are located at the centers of $t = 0$ and $1/2$, which are shown in black and gray, respectively.

satellite reflections. On the other hand, those obtained through the four-dimensional analyses showed good agreement with each other, even at high temperatures near the melting point, as seen in Fig. 10. This strongly indicates that at high temperatures beyond the phase separation (or in the thermal equilibrium), this Sb–Te compound is not an A7-type structure ($\gamma = 3/2$) itself but one of the homologous structures defined by $\gamma > 3/2$.

The present examination clarified that this Sb–Te compound has a long-period modulated structure like that of the aforementioned $\text{Sb}_{89}\text{Te}_{11}$. The modulation period γ kept a constant value of almost 1.5 up to a temperature of around 600 K, at which the oxidation of Sb started. However, above this temperature, just as in the $\text{Sb}_{89}\text{Te}_{11}$ case, γ grew larger with increasing temperature and reached a value of around 1.56 at high temperatures near the melting point (in contrast, in the previous experiment, Bragg peaks corresponding to AgInTe_2 were hardly observed for some reason). This γ value indicated that the composition of the compound should be ca $\text{Sb}_{87}\text{Te}_{13}$ [see equation (2)]. Here, we ignore the locations of Ag and In because they are minor elements. We carried out

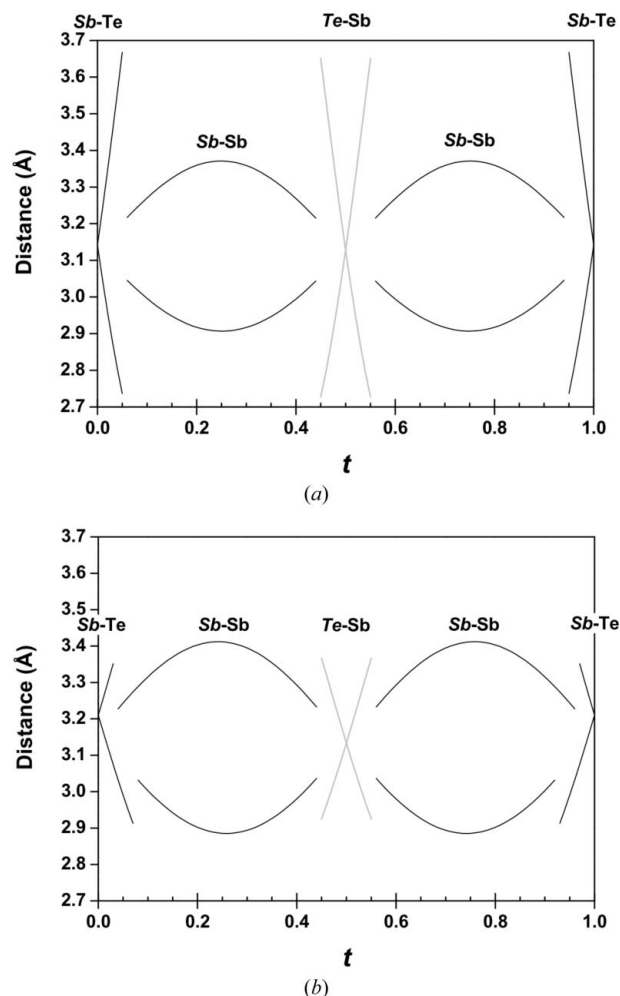


Figure 9
Interatomic distances versus t for $\text{Sb}_{89}\text{Te}_{11}$: (a) at 820 K near the melting temperature and (b) at 637 K just after phase decomposition. The central atoms are shown in italics.

Table 5

Final R factors for $\text{Sb}_{87}\text{Te}_{13}$ at 773 K obtained through four-dimensional Rietveld analyses performed assuming that it has (a) an incommensurately modulated structure (R factors for the entire pattern are $R_p = 0.0201$ and $R_{wp} = 0.0294$) and (b) a commensurately modulated structure.

The modulation period, γ , was maintained at $36/23$ during the refinements. The R factors for the entire pattern are: (b1) $R_{wp} = 0.0201$ and $R_p = 0.0294$ for $t_0 = 1/46 + n/23$ and (b2) $R_{wp} = 0.0251$ and $R_p = 0.0364$ for $t_0 = 0 + n/23$. The superspace group for $\text{Sb}_{87}\text{Te}_{13}$ was assumed to be $R\bar{3}m(00\gamma)00$ for both analyses; on the other hand, $Fd\bar{3}m$ was applied for Sb_2O_3 . The diffraction data used for the analysis: $3.0 \leq 2\theta \leq 30.5^\circ$. The standard deviations are shown in parentheses. B_i^* represents the positional modulation amplitude; U_s represent the atomic displacement parameters. Only the first satellites were considered for these analyses.

(a) Incommensurate case $\text{Sb}_{87}\text{Te}_{13}$:

R factors of profile and all reflections ($\text{Sb}_{89}\text{Te}_{11+}$)			
	RF_{obs}		0.0300
	R_{wp}		0.0189
R factors of profile and all reflections			
	RF_{obs}		0.0207
	R_{wp}		0.0106
R factors of satellites			
First order	RF_{obs}		0.0414
	RF_{wobs}		0.0325
Second order	RF_{obs}		0.0492
	RF_{wobs}		0.0280

$\gamma = 1.5660$ (5); $a = 4.3180$ (2), $c = 5.7268$ (4) Å.

Atom	g	x	y	z	B_1^*	B_2^*	U^{11} (Å ²)	U^{33} (Å ²)
Sb	1	0	0	0	-0.0306 (1)	0.0097 (3)	0.0368 (1)	0.0408 (1)
Te	1	0	0	0	-0.276 (3)	—	0.0368	0.0408

Sb_2O_3 ; $RF_{\text{obs}} = 0.0384$, $RF_{\text{wobs}} = 0.0343$, $a = 11.2470$ (6) Å.

Atom	Site	g	x	y	z	U_{iso} (Å ²)
Sb	4b	1.0	0.8870 (1)	x	x	0.026 (1)
O	8d	1.0	0.188 (2)	0	0	0.026

(b1) Commensurate case ($t_0 = \frac{1}{46} + \frac{n}{23}$; $n = 0, 1, 2, \dots$). $\text{Sb}_{87}\text{Te}_{13}$:

R factors of profile and all reflections ($\text{Sb}_{89}\text{Te}_{11+}$)			
	RF_{obs}		0.0293
	R_{wp}		0.0176
R factors of profile and all reflections			
Main	RF_{obs}		0.0192
	R_{wp}		0.0100
R factors of satellites			
First order	RF_{obs}		0.0424
	RF_{wobs}		0.0320
Second order	RF_{obs}		0.0472
	RF_{wobs}		0.0246

$\gamma = 36/23$; $a = 4.3181$ (2), $c = 5.7267$ (4) Å.

Atom	g	x	y	z	B_1^*	B_2^*	U^{11} (Å ²)	U^{33} (Å ²)
Sb	1.0	0	0	0	-0.0306 (1)	0.0105 (3)	0.0368 (1)	0.0413 (3)
Te	1.0	0	0	0	-0.285 (3)	—	0.0368	0.0413

Sb_2O_3 ; $RF_{\text{obs}} = 0.0360$, $RF_{\text{wobs}} = 0.0314$, $a = 11.2471$ (6) Å.

Table 5 (continued)

Atom	Site	g	x	y	z	U_{iso} (Å ²)
Sb	4b	1.0	0.8870 (1)	x	x	0.026 (1)
O	8d	1.0	0.188 (2)	0	0	0.026

(b2) Commensurate case ($t_0 = 0 + \frac{n}{23}$; $n = 0, 1, 2, \dots$). $\text{Sb}_{87}\text{Te}_{13}$:

R factors of profile and all reflections ($\text{Sb}_{89}\text{Te}_{11+}$)			
	RF_{obs}		0.0455
	R_{wp}		0.0257
R factors of profile and all reflections			
Main	RF_{obs}		0.0321
	R_{wp}		0.0155
R factors of satellites			
First order	RF_{obs}		0.0719
	RF_{wobs}		0.0636
Second order	RF_{obs}		0.0559
	RF_{wobs}		0.0246

$\gamma = 36/23$; $a = 4.3181$ (2), $c = 5.7275$ (5) Å.

Atom	g	x	y	z	B_1^*	B_2^*	U^{11} (Å ²)	U^{33} (Å ²)
Sb	1.0	0	0	0	-0.0243 (2)	0.0065 (3)	0.0382 (2)	0.0331 (4)
Te	1.0	0	0	0	-0.326 (2)	—	0.0382	0.0331

Sb_2O_3 ; $RF_{\text{obs}} = 0.0552$, $RF_{\text{wobs}} = 0.0358$, $a = 11.2478$ (8) Å.

Atom	Site	g	x	y	z	U_{iso} (Å ²)
Sb	4b	1.0	0.8871 (2)	x	x	0.021 (2)
O	8d	1.0	0.187 (3)	0	0	0.021

four-dimensional structural analyses for the two cases where this Sb–Te crystal took an incommensurately or commensurately modulated structure. As shown in Table 5 these analyses gave almost the same good results, when $\gamma = 36/23$ ($n = 9$, $m = 1$; $\text{Sb}_{87.0}\text{Te}_{13.0}$) was applied in the commensurate case (this three-dimensional structure model is shown in Fig. 7b). However, the results of the commensurate case could be considered somewhat better than those of the incommensurate case (cf. Table 5a with Table 5b1), in contrast to the examination of $\text{Sb}_{89}\text{Te}_{11}$. In addition, we can find a clear t_0 dependence of the R values in the results of the Rietveld analyses performed in the commensurate case (cf. Table 5b1 with Table 5b2). This strongly suggests that this $\text{Sb}_{87}\text{Te}_{13}$ compound eventually obtained a (probably stable) commensurate structure through rearrangement of the atoms from the A7-type atomic configuration after sufficient heat treatment for this material, as observed in the case of Sb_8Te_3 (Kifune *et al.*, 2011). Generally, the determination between the commensurate and incommensurate case seems to be beyond the information contained in our powder data. However, we believe that it is very likely that many of these compounds ultimately obtain commensurate structures after sufficient heat treatment. We intend to conduct further experiments and analyses for these materials to reveal their structural features more precisely.

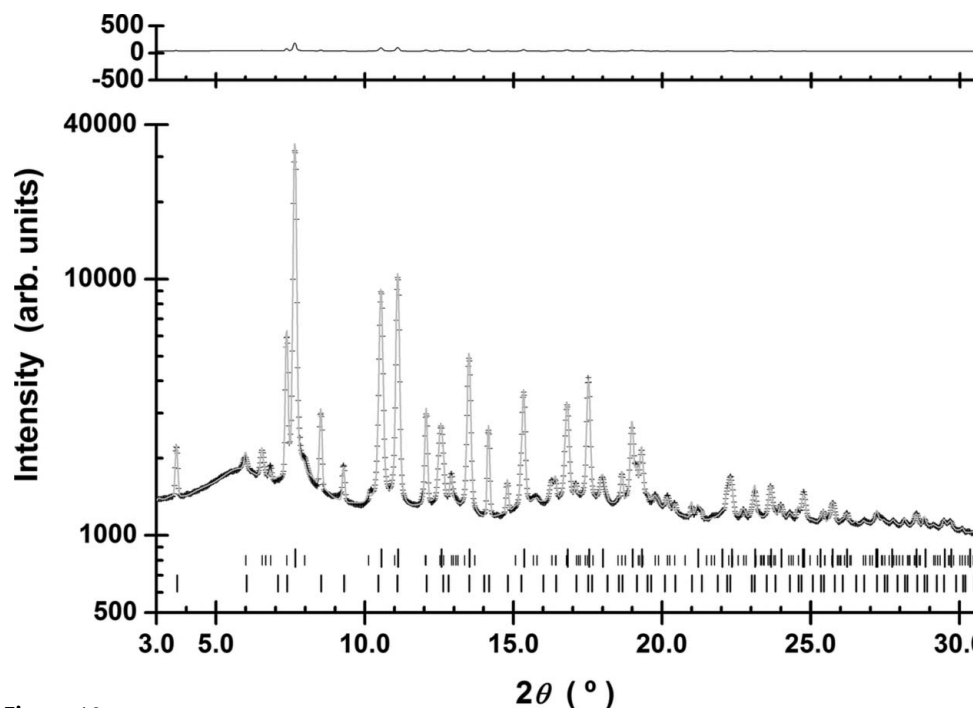


Figure 10

Observed (+) and calculated (gray line) X-ray diffraction profiles for $\text{Ag}_{3.4}\text{In}_{3.7}\text{Sb}_{76.4}\text{Te}_{16.5}$ ($\text{Sb}_{87}\text{Te}_{13}$ + Sb_2O_3) at 873 K by Rietveld analysis in the commensurate case (see Table 5b1). This diffraction data were obtained in 1999 at SPring-8 (Matsunaga *et al.*, 2001). A difference curve (observed – calculated) appears at the top of the figure; reflection markers are indicated by vertical spikes below the diffraction patterns. Of the first line of spikes the longer ones are for the peaks of the main reflections of $\text{Sb}_{87}\text{Te}_{13}$, and the shorter ones are for the satellites. Those at the bottom show the peak positions for Sb_2O_3 .

4. Conclusions

An $\text{Ag}_{3.4}\text{In}_{3.7}\text{Sb}_{76.4}\text{Te}_{16.5}$ quaternary amorphous film was first crystallized into an A7-type structure, in which the four types of atoms randomly occupied the atomic sites, right after the phase transformation. However, as the temperature was raised, this single crystalline phase separated into two crystalline phases, AgInTe_2 and an Sb–Te binary compound. Of these two crystals, AgInTe_2 was stable up to the melting point. In contrast, the latter crystal, $\text{Sb}_{89}\text{Te}_{11}$, had a modulated layer structure, and its modulation vector grew with an increasing in temperature.

The synchrotron radiation experiments were performed on BL02B2 at SPring-8 with the approval of the Japan Synchrotron Radiation Research Institute (proposal Nos. 2010B0084, 2010B1827 and 2011B0030). We express our sincere gratitude to Dr J. Kim at JASRI and to graduate students K. Shakudo, Y. Sato and T. Tachizawa of the Graduate School of Science at Osaka Prefecture University for their assistance with the experiments. The structural models in Fig. 7 were displayed using the Java Structure Viewer (*JSV* 1.08 lite) created by Dr Steffen Weber.

References

Clark, G. L. (1955). *Applied X-rays*. New York: McGraw-Hill.
Dušek, M., Petříček, V. & Palatinus, L. (2010). *J. Phys.* **226**, 012014.

Hoffmann, R. (1988). *Solids and Surfaces*. New York: VCH Publishers.

Iwasaki, H., Ide, Y., Harigaya, M., Kageyama, Y. & Fujimura, I. (1992). *Jpn. J. Appl. Phys.* **31**, 461–465.

Karpinsky, O. G., Shelimova, L. E., Kretova, M. A. & Fleurial, J.-P. (1998). *J. Alloys Compd.* **268**, 112–117.

Kifune, K., Fujita, T., Kubota, Y., Yamada, N. & Matsunaga, T. (2011). *Acta Cryst.* **B67**, 381–385.

Kifune, K., Kubota, Y., Matsunaga, T. & Yamada, N. (2005). *Acta Cryst.* **B61**, 492–497.

Kuznetsova, L. A., Kuznetsov, V. L. & Rowe, D. M. (2000). *J. Phys. Chem. Solids*, **61**, 1269–1274.

Lind, H. & Lidin, S. (2003). *Solid State Sci.* **5**, 47–57.

Matsunaga, T., Akola, J., Kohara, S., Honma, T., Kobayashi, K., Ikenaga, E., Jones, R. O., Yamada, N., Takata, M. & Kojima, R. (2011). *Nat. Mater.* **10**, 129–134.

Matsunaga, T., Kojima, R., Yamada, N., Fujita, T., Kifune, K., Kubota, Y. & Takata, M. (2010). *Acta Cryst.* **B66**, 407–411.

Matsunaga, T., Kojima, R., Yamada, N., Kifune, K., Kubota, Y., Tabata, Y. & Takata, M. (2006). *Inorg. Chem.* **45**, 2235–2241.

Matsunaga, T., Kojima, R., Yamada, N., Kifune, K., Kubota, Y. & Takata, M. (2007a). *Appl. Phys. Lett.* **90**, 161919–1–3.

Matsunaga, T., Kojima, R., Yamada, N., Kifune, K., Kubota, Y. & Takata, M. (2007b). *Acta Cryst.* **B63**, 346–352.

Matsunaga, T., Kojima, R., Yamada, N., Kifune, K., Kubota, Y. & Takata, M. (2008). *Chem. Mater.* **20**, 5750–5755.

Matsunaga, T., Morita, H., Kojima, R., Yamada, N., Kifune, K., Kubota, Y., Tabata, Y., Kim, J.-J., Kobata, M., Ikenaga, E. & Kobayashi, K. (2008). *J. Appl. Phys.* **103**, 093511–1–9.

Matsunaga, T., Umetani, Y. & Yamada, N. (2001). *Phys. Rev. B*, **64**, 184116–1–7.

Matsunaga, T. & Yamada, N. (2004a). *Phys. Rev. B*, **69**, 104111–1–8.

Matsunaga, T. & Yamada, N. (2004b). *Jpn. J. Appl. Phys.* **43**, 4704–4712.

Matsunaga, T., Yamada, N., Kojima, R., Shamoto, S., Sato, M., Tanida, H., Uruga, T., Kohara, S., Takata, M., Zalden, P., Bruns, G., Sergueev, I., Wille, H. C., Hermann, R. P. & Wuttig, M. (2011). *Adv. Funct. Mater.* **21**, 2232–2239.

Matsunaga, T., Yamada, N. & Kubota, Y. (2004). *Acta Cryst.* **B60**, 685–691.

Nishibori, E., Takata, M., Kato, K., Sakata, M., Kubota, Y., Aoyagi, S., Kuroiwa, Y., Yamakata, M. & Ikeda, N. (2001). *Nucl. Instrum. Methods A*, **467–468**, 1045–1048.

Petříček, V. & Dušek, M. (2000). *JANA2000*. Institute of Physics, Praha, Czech Republic.

Petříček, V., Dušek, M. & Palatinus, L. (2006). *JANA2006*. Institute of Physics, Praha, Czech Republic.

Poudeu, P. F. P. & Kanatzidis, M. G. (2005). *Chem. Commun.* pp. 2672–2674.

Rietveld, H. M. (1969). *J. Appl. Cryst.* **2**, 65–71.

Shelimova, L. E., Karpinskii, O. G., Konstantinov, P. P., Avilov, E. S., Kretova, M. A. & Zemskov, V. S. (2004). *Inorg. Mater.* **40**, 530–540.

- Shelimova, L. E., Karpinskii, O. G., Konstantinov, P. P., Kretova, M. A., Avilov, E. S. & Zemskov, V. S. (2001). *Inorg. Mater.* **37**, 342–348.
- Shelimova, L. E., Karpinskii, O. G., Zemskov, V. S. & Konstantinov, P. P. (2000). *Inorg. Mater.* **36**, 235–242.
- Shelimova, L. E., Konstantinov, P. P., Karpinsky, O. G., Avilov, E. S., Kretova, M. A. & Zemskov, V. S. (2001). *J. Alloys Compd.* **329**, 50–62.
- Wolff, P. M. de (1974). *Acta Cryst.* **A30**, 777–785.
- Wolff, P. M. de, Janssen, T. & Janner, A. (1981). *Acta Cryst.* **A37**, 625–636.
- Wuttig, M. & Yamada, N. (2007). *Nat. Mater.* **6**, 824–832.
- Wyckoff, R. W. G. (1986). *Crystal Structures*, Vol. 2. Florida: Robert E. Krieger Publishing Company.
- Yamada, N., Ohno, E., Nishiuchi, K., Akahira, N. & Takao, M. (1991). *J. Appl. Phys.* **69**, 2849–2856.